

Femtosecond Laser-induced Porosity on Poly(ethylene) Surfaces – a Crystallographic and Rheological Study

Youssef Assaf^a, Mark Zhao^a, and Anne-Marie Kietzig^{a*}

^aDepartment of Chemical Engineering, McGill University, 3610 University Street, Montreal, Canada, H3A 0C5

Youssef Assaf: +1(514) 946-8893; youssef.assaf@mail.mcgill.ca

Mark Zhao: +1(438) 345-3182; mark.zhao@mail.mcgill.ca

*Anne Kietzig (corresponding author): +1(514) 398-3302; anne.kietzig@mcgill.ca

Abstract

In recent years, femtosecond (fs) laser irradiation of polymer surfaces has been shown to produce novel porous topologies that present a multi-scale roughness. In our study, grazing incidence x-ray diffractometry (GIXRD) results showed the appearance of a monoclinic crystalline phase on fs laser machined high density polyethylene (HDPE) which is a deformation of the orthorhombic phase typically observed in pristine HDPE. This was accompanied with a local decrease in crystallinity. These findings confirmed that the induced porosity was a consequence of the rapid quenching of a superheated melt layer undergoing phase explosion. In addition, several poly(ethylene) samples with different average molecular weights were machined under the same conditions. Scanning electron micrography, along with small angle oscillatory shear tests, indicated that final pore size decreases with increasing average molecular weight or increasing melt viscosity since these parameters act against bubble growth during phase explosion. In addition, through computed tomography, the internal structure of the porous layer was investigated. Through this technique, the average pore size and pore size distribution can be computed by chord length analysis. In conclusion, in this study, the mechanisms behind the formation of femtosecond laser-induced porous structures and the parameters that control their dimensions have been established.

Keywords

Femtosecond laser; polymer; porosity; x-ray diffraction; rheometry; computed tomography

1. INTRODUCTION

Polymer surfaces have traditionally been difficult to process by laser machining due to their low absorption [1]. With the advent of femtosecond (fs) technology, polymer machining is now possible through non-linear optical processes such as multiphoton absorption [2]. This now allows the inscription of precise micrometric geometries on polymer surfaces. Precise ablation has allowed the fabrication of polymeric surfaces for lab-on-chip applications [3], Fresnel lenses [4], and intraocular lenses [5] among others. In contrast with such laser inscribed structures, femtosecond laser-induced (or self-assembled) microstructures have recently been of interest. Indeed, fs irradiation is known to produce a multiscale micro/nano roughness on several types of

materials which is advantageous for the manipulation of their wettability [6-9]. In the case of polymers, the structure that has been most commonly reported is fs laser-induced porosity. This phenomenon was initially observed on the side walls of inscribed lines and holes on poly(methyl methacrylate) (PMMA) and poly(carbonate) (PC) [10, 11]. Since then, homogeneous polymer irradiation under certain conditions has been shown to cause the formation of a porous microstructure over the whole surface [7, 12, 13]. The resulting increase in surface area can be greatly beneficial for a number of applications such as omniphobic materials [13] or biomedical implants [14]. For example, Castillejo et al. have reported preferential fibroblast attachment and growth on a fs laser-induced porous structure produced on chitosan and starch [15]. Similar results for fibroblast cells were also reported by Daskalova et al. on porous structures produced by fs laser machining on collagen, gelatin, and elastin [16]. However, not much is known regarding the mechanism behind the formation of fs laser-induced porous structures which limits their optimization for specific applications.

So far, several authors have hypothesized that the porous topology forms as a consequence of explosive boiling. This phenomenon, also termed as phase explosion, occurs in the melt layer that forms beneath the ionized material during the ablation process. If the laser fluence is sufficiently high and the pulse duration sufficiently short, this melt layer can theoretically heat up above a certain critical temperature T_c where homogeneous bubble formation occurs [17]. Efthimiopoulos et al.'s study was the first to suggest that the porosity induced on PMMA after irradiation is related to the bubble formation during boiling [18]. Baudach et al. later suggested that the side wall porosity they observed in ablated craters on PMMA and PC are due to the same mechanism [19]. The theoretical plausibility of this hypothesis on PMMA was also validated by the numerical simulations performed by Guay et al. [20]. In our previous work, we further suggested that this phenomenon can occur on any polymer as long as its threshold fluence is large enough so that the melt layer is heated past T_c [12]. In summary, during femtosecond laser polymer ablation, energy delivery to the surface and subsequent boiling happens in the order of picoseconds [21]. The high rate of heating leads to the formation of a melt layer that is almost immediately quenched to room temperature between two consecutive pulses. The melt thus re-solidifies in the shape of a porous layer with the pores being a remnant of the volume occupied by the bubbles during phase explosion. While this theory seems to be generally accepted today, the timescale involved in the formation of these structures is too short to visualize the process directly. Thus,

experimental evidence of melt re-solidification needs to be retroactively measured from a change in surface properties. In crystalline polymers, rapid melt and quenching should have an effect on the crystallinity and/or crystal structure since the high cooling rate limits the time available for crystal formation and growth. The only measurements on the effect of femtosecond laser irradiation on polymer crystallinity were performed on amorphous PLA where, as expected, crystallinity was not induced during machining [22, 23].

Another relatively unexplored aspect related to these microstructures is the dimension of the pore size. If it is indeed related to bubble growth during boiling, then pore size should inevitably be related to the viscoelastic properties of the melt layer. Rebollar et al. have previously observed that the size of surface swelling bubbles after nanosecond laser irradiation of PMMA is inversely proportional to average molecular weight M_w [24]. They explained this correlation by stating that polymers with lower M_w are less viscous when melted and offer more free volume. This would promote bubble growth to larger sizes. So far, no other study reported this phenomenon and it is unclear if the same phenomenon applies to laser-induced porous structures on polymer surfaces. Another parameter that could affect pore size is the laser fluence. In their study on PMMA, Baset et al. suggest that the porosity observed on the bottom or side walls of ablated craters depends on the incoming laser power [11]. With increasing power, more pores were observed to appear but their size diminished. In our two recent studies, the effect of fluence on laser-induced microstructure on several polymers was investigated [12, 25]. While some polymers had their texture affected at high fluence, pore size was observed to be mostly unaffected by this parameter. The reason behind this discrepancy could be attributed to the very high accumulated fluence values achieved when producing laser-induced structures over a large area, as opposed to crater inscription.

Finally, the quantification of femtosecond laser induced porosity remains a challenge for several reasons. First of all, the previously mentioned studies all report pore sizes of up to a few μm at most. Furthermore, this microstructure is typically less than 50 μm thick [13, 25] and rests atop the bulk non-modified polymer. This renders techniques such as porosimetry inapplicable since it would be nearly impossible to separate the modified surface layer from the non-modified bulk. In addition, there is no evidence that the pores are interconnected. As a consequence, even if the surface layer were to be somehow separated from the bulk, any intrusive technique would

ignore pores formed within the volume of the structure. Thus, a method to adequately quantify femtosecond laser induced porosity is still lacking.

In this study, the effect of femtosecond laser machining on the crystallinity and crystallographic structure of high density poly(ethylene) (HDPE) is studied. In addition, six different poly(ethylene) (PE) samples with increasing M_w and different melt viscosities were machined to see if pore size is indeed correlated to these properties. The internal structure of the porous layer formed after machining was also investigated by computed tomography. These experiments will therefore greatly contribute to our understanding of the formation of femtosecond laser induced microstructures thus allowing future pore size optimization for specific applications

2. MATERIALS AND METHODS

2.1 Materials:

Seven different grades of poly(ethylene) were used in this study. For GIXRD, 4*4 cm square samples were cut from a 1.5 mm thick HDPE sheet (Grade 1) purchased from McMaster-Carr. For this particular measurement, a poly(ethylene) grade with high density was chosen because of its high crystallinity which makes changes to its crystallographic structure easily detectable. Measurements were done on two samples: a non-modified pristine sample and a laser machined sample. They will be referred to as 1-P and 1-L respectively.

For all other experiments, six PE grades with increasing average molecular weights were used. Samples were compression molded from pellets or powders (Sigma Aldrich) into 2.54 cm diameter discs with 1 mm thickness at 150°C and 5 metric tonnes of pressure for 15 minutes. Table I presents the properties of the six PE grades used for these experiments as well as the sample number assigned to them. Weight average molecular weights M_w were measured by GPC as described in section 2.5 and density values ρ were provided by the supplier. The M_w range for the ultra high molecular weight (UHMW) sample was also provided by the supplier because its viscosity lied outside the measurement range of the HT-GPC setup used.

Table I: Densities and weight average molecular weights of PE grades used for rheometry experiments.

Grade number	M_w (kg/mol)	ρ (g/cm ³)
2	5	0.92
3	9	0.94
4	39	0.906
5	55	0.925
6	59	0.952
7	3×10^3 - 6×10^3	0.94

2.2 Laser micromachining:

A solid state Ti:sapphire laser system (Coherent Libra) delivering a Gaussian beam at a wavelength of 800 nm and in pulses of 150 fs duration operated at a repetition rate f_p of 1 kHz was used for all micromachining experiments. The 4 W beam passes through a digitally controlled attenuator consisting of a half-wave plate and a polarizing beam splitter in order to lower its power down to the desired value P . It then passes through a digitally controlled mechanical shutter (Uniblitz) before being focused onto the sample through a 100 mm lens down to a 44 μ m spot size ω_0 . The sample rests atop a 3D stage (Newport Corporation) whose trajectory and velocity v are controlled by the GOL3D software (GBC&S). All laser-induced microstructures were produced by raster scanning the beam with a spatial overlap Φ of 0.95, a pulse-per-spot number PPS of 55, and a single pulse peak fluence F_0 of 3.3 J/cm². F_0 and PPS were calculated from processing parameters using the following equations:

$$F_0 = \frac{8P}{\pi\omega_0^2 f_p} \quad (1)$$

$$PPS = \frac{\omega_0 f_p}{v(1-\Phi)} \quad (2)$$

2.3 Scanning electron microscopy:

All samples were cleaned in a sonication ethanol bath for 5 mins immediately after machining in order to get rid of any loose machining debris. The surface structure was imaged by a scanning electron microscope (SEM) (FEI Inspect F50). This involved sputter coating (SPI-Module, Structure Probe Inc.) the samples with a 10 nm layer of gold in order to avoid surface charging.

2.4 Grazing incidence x-ray diffraction (GIXRD):

GIXRD scans were performed using a Bruker D8 Discovery diffractometer equipped with a Cu-K α source ($\lambda=0.154$ nm) and a HiSTAR area detector. A depth profile of the samples was performed by varying the incident angle θ from 10^0 to 0.2^0 in order to vary the penetration depth of the x-ray beam. This way, the crystallographic structure of the bulk and modified surface layer can be compared. A 15 min step-scan in increments of 0.02^0 2θ over a $1*1$ mm area of the sample was performed at each incident angle. Crystallinity was determined by calculating the relative area of the crystalline peaks and amorphous background with respect to the total area under the intensity curve.

2.5 Gel permeation chromatography:

The average molecular weights M_w of grades 2 to 7 were determined using a Viscotek 350 (Malvern Panalytical) high temperature gel permeation chromatography (HT-GPC) setup equipped with 3 PLgel mixed organic columns (Agilent). Calibration was performed using a broad molecular weight range polystyrene standard kit (Scientific Polymer Products, Inc.). Each sample was dissolved in trichlorobenzene (containing 500 ppm of butylatedhydroxytoluene) at a concentration of 2 mg/mL. The measurements were performed at 140^0 C using a 200 μ L injection volume and a flowrate of 1 mL/min.

2.6 Rheometry:

All measurements were performed using a strain-controlled Anton-Paar MCR 302 rheometer set up with a parallel plate stainless steel accessory (25 mm diameter) and a CTD 450 convection oven heated to 190^0 C. For each sample, both an oscillatory shear test and a ramping rotational shear test were performed. For the oscillatory measurements, a preliminary amplitude

sweep was performed on all samples from 0.01% to 100% strain amplitude γ_0 . As a consequence, all experiments were performed at a strain amplitude of 1% as the value falls within the viscoelastic range for all samples. Subsequently, a frequency sweep, where the angular frequency ω was varied from 0.3 to 300 rad/s, was performed on all samples in order to measure the storage and loss moduli G' and G'' as well as the complex viscosity η^* . For the ramping measurements, the dynamic viscosity η was measured while increasing the strain rate $\dot{\gamma}$ from 0.01 to 100 s⁻¹.

2.7 Computed tomography:

Computed tomography (CT) was performed using an Xradia 520 Versa (Zeiss) with a spatial resolution of 0.7 μm . 3D reconstruction and slicing was performed using the Dragonfly software (Object Research Systems). The porosity was calculated by the software by measuring the volume ratio of pore voxels to total (pore and solid) voxels. For the calculation of pore size distribution, 10 slices separated by a distance of 1 μm were analyzed. They were first thresholded using Yen's algorithm in order to separate them into black (pores) and white (solid) pixels [26]. Each slice was then both horizontally and vertically scanned and the chord length of the pores (number of consecutive black pixels) was calculated using a Matlab (MathWorks) code.

3. RESULTS AND DISCUSSION

First, a comparison between the crystal structure of non-modified and laser machined HDPE was performed in order to look for evidence of melt resolidification and thus validate the hypothesis that explosive boiling is the mechanism responsible for the resulting porous structures. Subsequently, the effect of increasing molecular weight on laser-induced pore size and the internal structure of the modified surface layer were investigated. Finally, the results were explained by measuring the change in viscoelastic properties with increasing molecular weight through rheometry analysis and evaluating how it would affect explosive boiling during laser machining.

3.1 Effect of laser machining on crystal structure:

Figure 1 shows the micrographs for non-modified (1-P) and laser machined (1-L) HDPE, while Figure 2 represents the resulting large incident angle GIXRD scans.

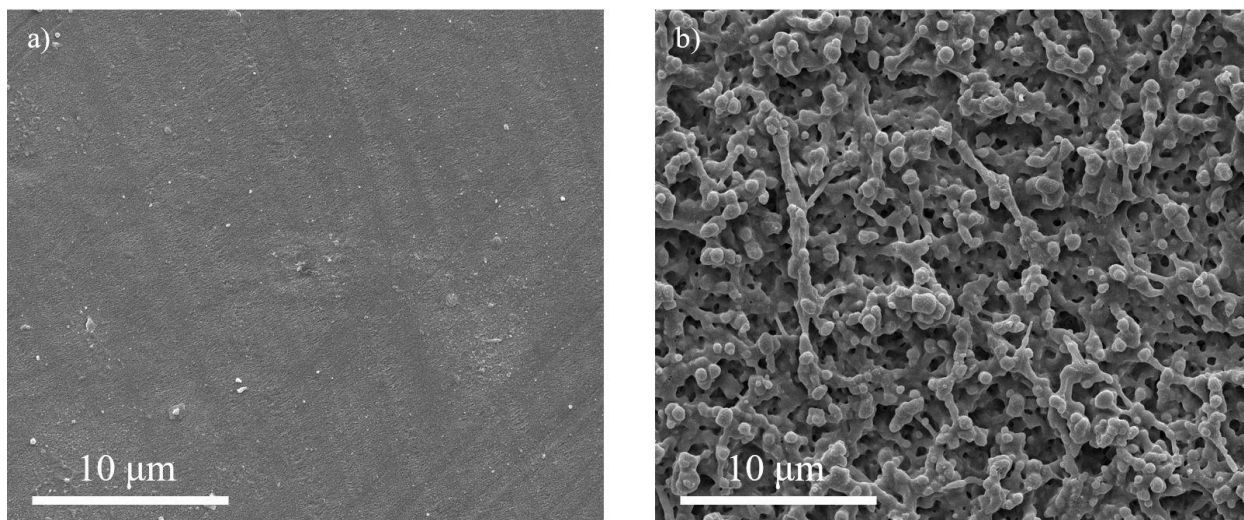


Figure 1: SEM micrographs for samples a) 1-P and b) 1-L

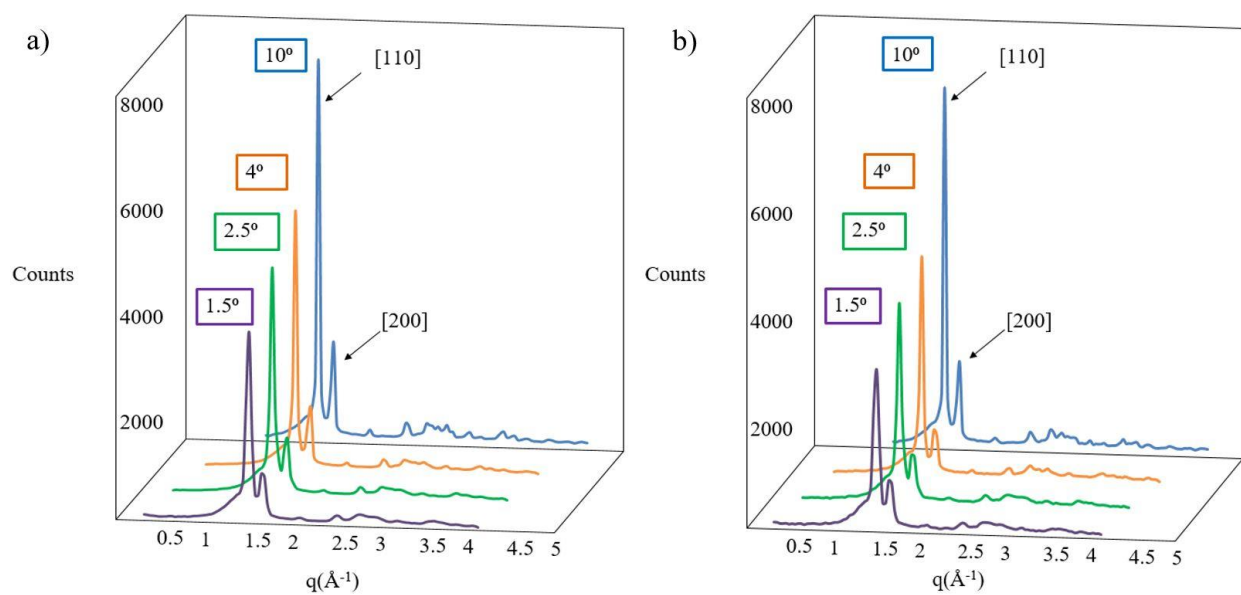


Figure 2: GIXRD scans for large incident angles on samples a) 1-P and b) 1-L.

Looking at Figure 2a, it is apparent that our HDPE sample is semi-crystalline as seen from the presence of two sharp peaks. The signals strongly indicate that the crystalline region is arranged in the typical orthorhombic structure with $Pnam$ spacing that is characteristic of HDPE (Figure 4a)

[27]. Thus, the large peak at 1.53 \AA^{-1} corresponds to the reflection from the [110] plane, while the smaller peak at 1.69 \AA^{-1} corresponds to the reflection from the [200] plane [28, 29]. By comparing the results from sample 1-P (Figure 2a) to those from sample 1-L (Figure 1b), it is evident that the results are almost identical. This is in contrast with the results from scans at low incident angles as illustrated in Figure 3.

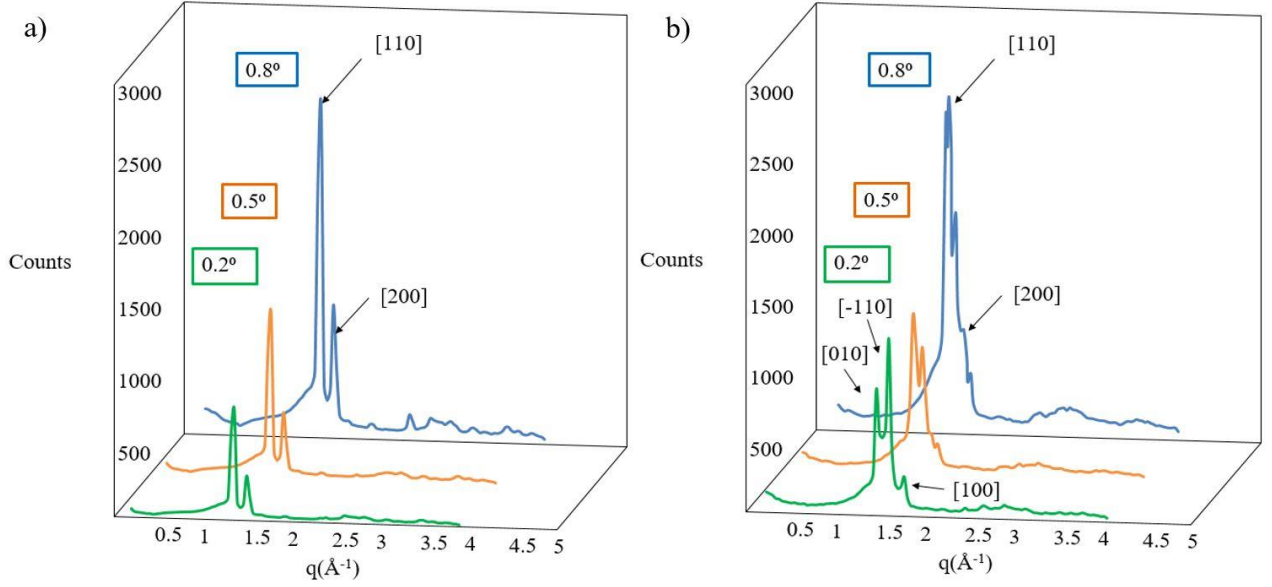


Figure 3: GIXRD scans for small incident angles on samples a) 1-P and b) 1-L.

Figure 3a shows no difference in crystallographic structure for sample 1-P between the scans at low and high incident angles. This indicates that the HDPE in question has a relatively homogeneous crystalline structure throughout its depth profile, even in the first few layers underneath the surface. On the other hand, Figure 3b clearly indicates that, for sample 1-L, new peaks can be identified for incidence angles below 1.5° . For an incident angle of 0.8° , the [110] and [200] reflections of the orthorhombic structure are still present. However, three new peaks appear located at 1.47 \AA^{-1} , 1.6 \AA^{-1} , and 1.77 \AA^{-1} . As the incident angle decreases, the orthorhombic peaks gradually recede until only the three new peaks are left at 0.2° . This is a clear indication of the formation of a new crystalline phase after machining. The combination of these three peaks is consistent with the reflections from the [010], [-110], and [100] planes of a monoclinic structure with $P2_1/m$ spacing (Figure 4b) [30]. This phase is similar to the orthorhombic one except for one of the lattice vectors not being orthogonal to the other two. This distortion of the orthorhombic arrangement is only formed and stable at high temperatures and pressures (typically above 6 GPa

at 280⁰ C) and typically reverts back at room temperature [30]. It arises due to tensile or compressive stresses above the yield point of the material [31]. The ultrashort timescale of energy delivery during femtosecond laser machining has been reported to induce very high local pressures and temperatures. For dielectrics such as silica, Hu et al. have calculated local pressures to be in the TPa range for the ionized layer [32]. In addition, Bulgakova et al. have demonstrated that the underlying melt layer will be superheated to temperatures of several thousand Kelvin and subjected to tensile stresses of several dozen MPa [33] which are conditions that can lead to homogeneous bubble formation as demonstrated by Bellouard et al. [34]. Therefore, we conclude that femtosecond laser micromachining of HDPE can lead to the conditions necessary for the formation of the monoclinic phase. However, the fact that it was still present at room temperature can only mean that the superheated melt layer was very rapidly quenched, thus preventing it from reverting to the orthorhombic phase. In order to check this hypothesis, the samples were annealed at 105⁰ C for 24 hours to check if the orthorhombic phase would be recovered. The annealed pristine sample and annealed laser machined sample will be referred to as 1-PA and 1-LA respectively. Figure 5 presents the GIXRD results at low incidence angles for the annealed samples.

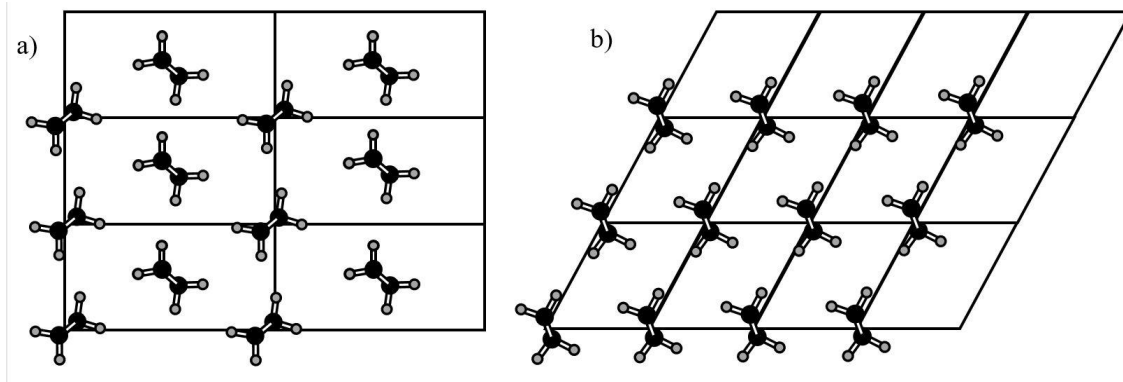


Figure 4: Top view of a) orthorhombic PE crystal with $Pnam$ spacing and b) monoclinic PE crystal with $P2_1/m$ spacing. Adapted from [30].

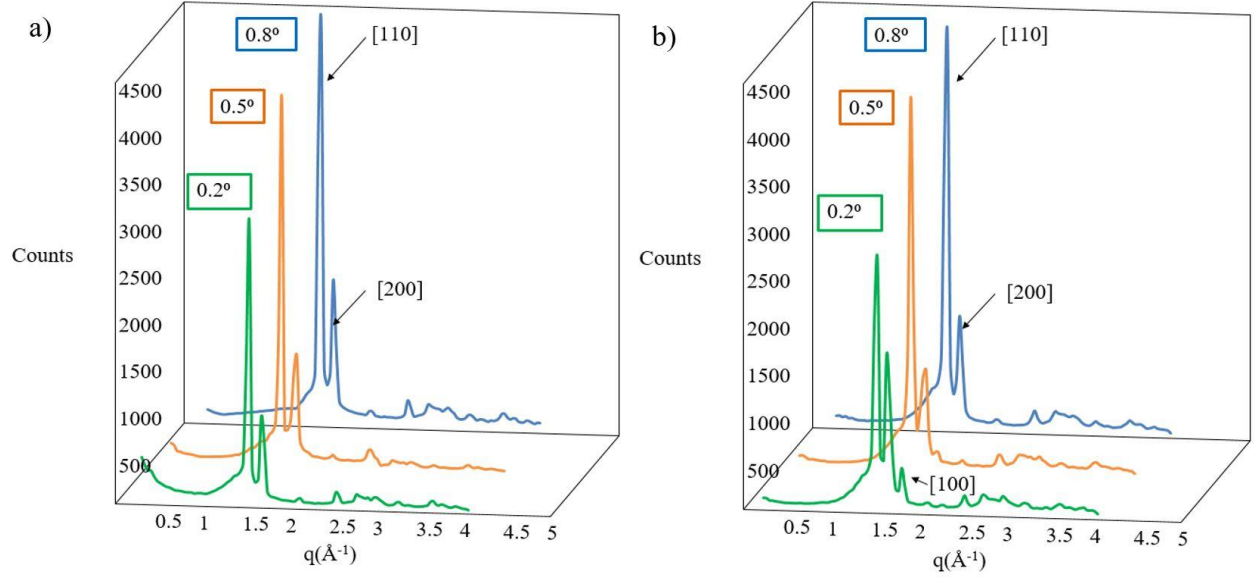


Figure 5: GIXRD scans for small incident angles on samples a) 1-PA b) 1-LA.

The results for sample 1-LA (Figure 5b) show a complete recovery of the orthorhombic phase at an incident angle of 0.8° . At $\theta=0.2^\circ$, the orthorhombic phase is prevalent even if a small amount of residual monoclinic phase subsides. The recovery of the original crystalline structure of the material by annealing confirms that the peak identification was correct and that femtosecond laser machining of HDPE does indeed induce the formation of a monoclinic phase. For sample 1-PA (Figure 5a), the only noticeable change is that peak intensity increases after annealing. Table II summarizes the crystallinity values computed from all GIXRD measurements.

Table II: Effect of laser machining and annealing on crystallinity for Grade 1.

$\theta(^{\circ})$	1-P (% Crystallinity)	1-PA (% Crystallinity)	1-L (% Crystallinity)	1-LA (% Crystallinity)
10	55	72	54	69
4.0	54	70	53	69
2.5	52	68	52	70
1.5	54	71	52	68
0.8	54	68	44	58
0.5	52	71	46	58
0.2	52	69	45	57

Sample 1-P's crystallinity was measured to be around 53%. For $\theta > 1.5^\circ$, machining did not have a significant effect on crystallinity as seen from the measurements for sample 1-L. This was expected since these measurements come from the bulk material beneath the modified layer. In the modified layer ($\theta < 1.5^\circ$), the average crystallinity dropped to 45%. This means that, despite the appearance of a new crystalline phase, the polymer became more amorphous overall. This is consistent with a rapid melting and quenching mechanism. Finally, as expected, annealing increased the crystallinity for all measurements by more than 10% as observed for samples 1-PA and 1-LA.

In conclusion, GIXRD measurements confirm that the femtosecond-laser induced porous microstructures are formed from the resolidification of a rapidly quenched superheated melt. In this case, the viscoelastic properties of the melt should have a significant effect on bubble growth during boiling and thus on the final laser-induced pore size. Since the viscoelastic properties of polymer melts are dictated by their molecular weight, the effect of M_w on laser-induced porous structures was investigated next.

3.2 Effect of molecular weight on laser-induced porous structures:

All grades listed in Table I were laser machined as described in section 2.6. Figure 6 presents the resulting SEM micrographs.

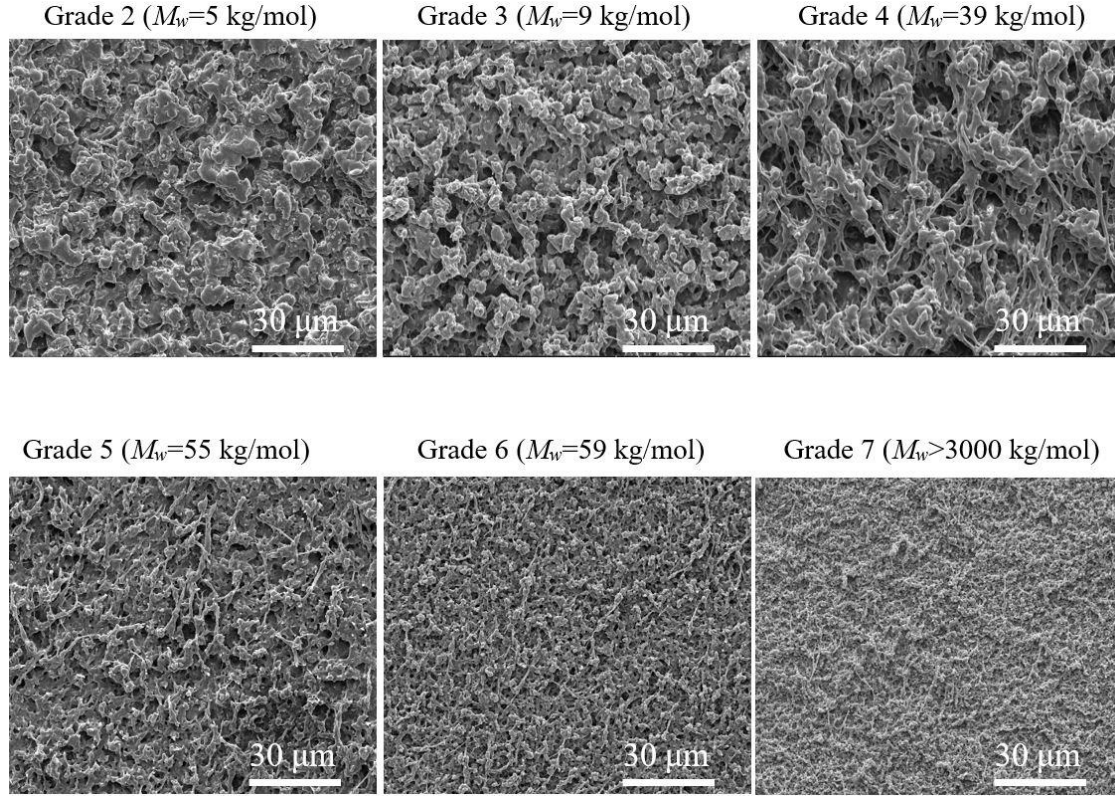


Figure 6: Decrease in pore size with increasing average molecular weight.

By looking at the different micrographs, it is apparent that molecular weight seems to have a significant effect on laser-induced pore size. With the exception of the two grades with the lowest M_w (grades 2 and 3), increasing molecular weight from grade 4 to grade 7 seems to correlate with decreasing pore size. In order to further investigate the internal structure of such laser modified surface layers, computed tomography was performed on the femtosecond laser-induced microstructure produced on grade 4 (Figure 7).

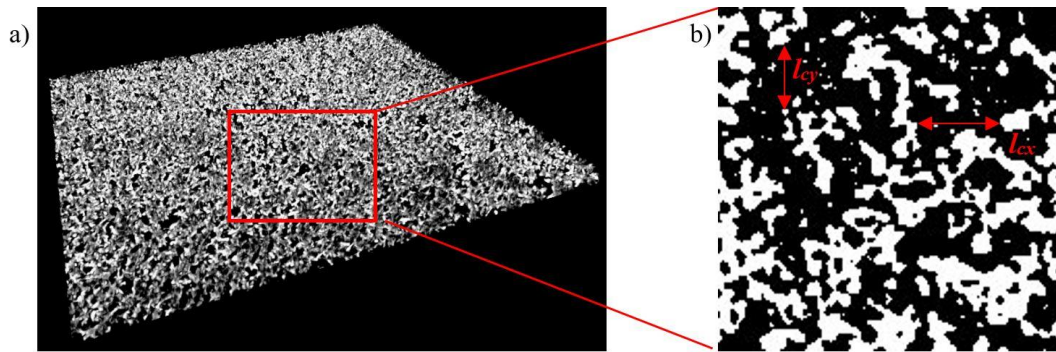


Figure 7: a) Computed tomography 3D reconstruction of a $700 \times 700 \times 10 \mu\text{m}^3$ volume located inside the laser-induced surface microstructure on grade 4 and b) $150 \times 150 \mu\text{m}^2$ thresholded area with example measurements of horizontal chord length l_{cx} and vertical chord length l_{cy} .

As can be seen in the 3D reconstruction, computed tomography successfully recreated the internal structure of the laser modified surface layer. By comparing solid voxel volume to total volume, the porosity can be calculated with the value for the particular volume shown in Figure 7 being 55%. Furthermore, the reconstruction showed that most of the pores are interconnected within the microstructure. Thus, traditional pore size analysis is not possible and we resorted to chord length measurements as described in section 2.7 and illustrated in Figure 7b. Figure 8 exemplarily presents chord length distributions for the horizontal and vertical directions for the volume shown in Figure 7.

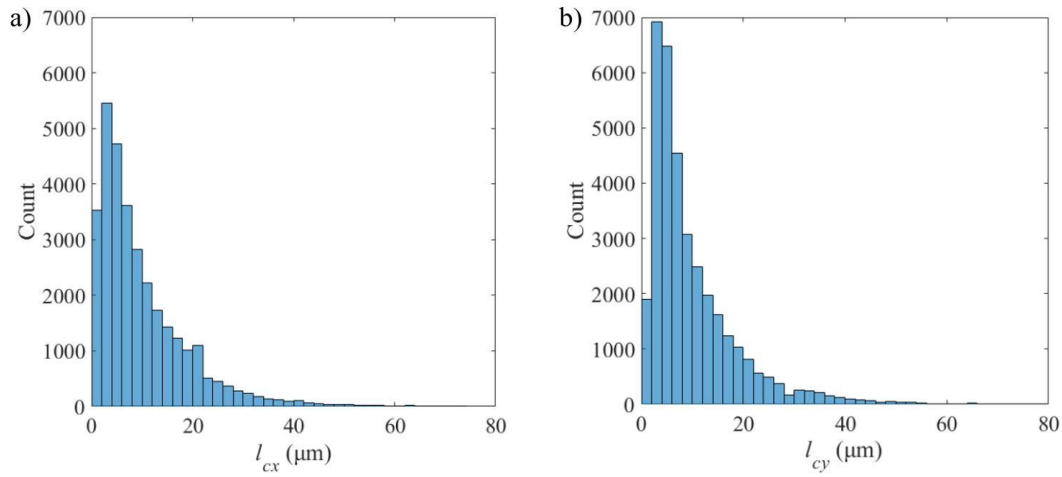


Figure 8: a) Horizontal and b) vertical chord length distributions for the laser induced structure produced on grade 4.

By comparing Figure 8a and 8b, the horizontal and vertical chord length distributions appear to be similar with most lengths falling in between 2 and 4 μm . Thus, the pores can be said to have similar sizes and seem to be homogeneously distributed throughout the modified volume. These results can only be explained by evaluating how M_w affects the viscoelastic melt properties and therewith bubble growth during femtosecond laser-induced explosive boiling. Thus, as a final step, the viscoelastic properties of the samples in question were measured by rheometry analysis.

3.3 Effect of viscoelastic properties on laser-induced pore size:

Figure 9 presents the viscosity results from both the oscillatory and ramping shear tests on all grades listed in Table I. Since all measurements were taken at a temperature of 190⁰ C, they cannot be used to quantitatively describe melt flow behavior during femtosecond laser machining. Indeed, as previously mentioned, the temperatures reached during machining can be an order of

magnitude higher, which would lead to much lower viscosities. However, the ranking of the six grades from least viscous to most viscous can still be used as a qualitative assessment of melt flow properties at high temperatures.

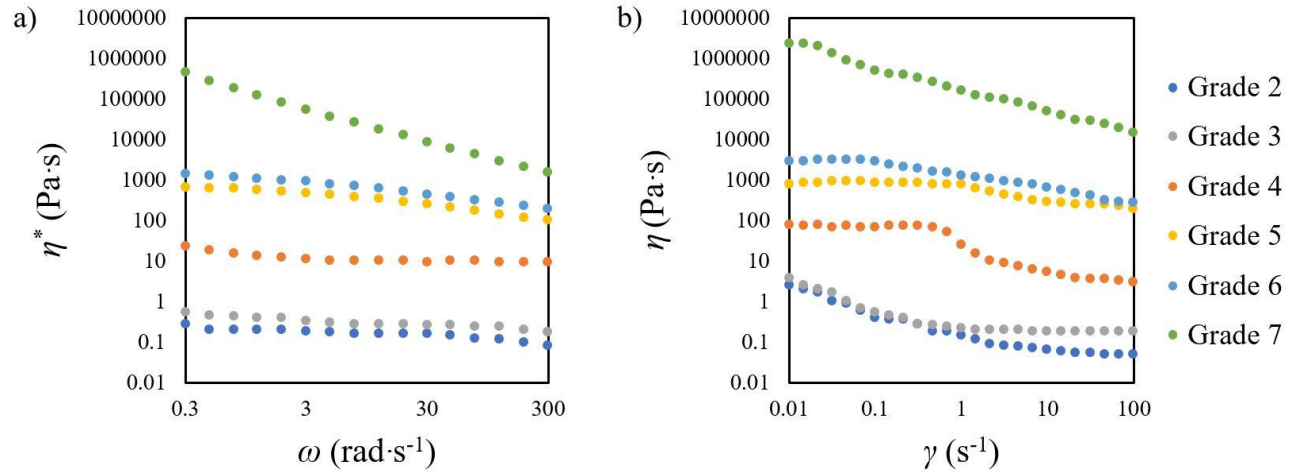


Figure 9: a) Complex viscosity versus angular frequency and b) dynamic viscosity versus shear rate at 190⁰ C.

Both tests gave similar results with respect to viscosity. All grades experienced some kind of shear thinning behavior as their viscosity decreased with increasing angular frequency or shear rate. Looking back at Table I, as expected, viscosity increased by orders of magnitude with increasing molecular M_w . Table III summarizes these results in addition to the G' and G'' values.

Table III: Viscoelastic properties at 190⁰ C, $\omega=1$ rad·s⁻¹, and $\gamma=1$ s⁻¹.

Grade number	η^* (Pa·s)	η (Pa·s)	G' (Pa)	G'' (Pa)
2	0.2	0.15	0.081	0.227
3	0.4	0.2	0.23	0.4
4	13	25	1.4	2.1
5	552	759	156	641
6	1100	1310	426	1240
7	123000	160000	140000	43100

In summary these grades can be grouped into three categories based on their melt viscoelastic properties: I-low viscosity grades (grades 2, 3, and 4), II-moderate viscosity grades (grades 5 and 6), and III- high viscosity grades (grade 7). By looking at the moduli, in the first group, viscous dissipation is prevalent and there is limited resistance to flow. In contrast, grade 7 offers significant flow resistance as elastic recovery is dominant. Finally, group II offers flow properties that are somewhere in between.

If we consider bubble growth dynamics in viscoelastic melts, then the correlation between increasing M_w and decreasing pore size observed in Figure 6 can be explained. No physical model to describe bubble growth induced by the extreme heating rates achieved during femtosecond laser machining has been proposed yet. However, a qualitative description of the parameters that affect it can be made by considering homogeneous spherical bubble growth in a viscoelastic liquid. This can be described by the adapted Rayleigh-Plesset equation [35]:

$$R \frac{d^2R}{dt^2} + \frac{3}{2} \left(\frac{dR}{dt} \right)^2 = \frac{1}{\rho_l} (P_g - P_\infty) - 4 \frac{\eta_l}{R} \frac{dR}{dt} - \frac{2\sigma}{\rho_l R} - \frac{E}{\rho_l} \quad (3)$$

Where R is the bubble radius, t is time, ρ_l is the density of the liquid, P_g is the pressure inside the bubble, P_∞ is the external pressure, η_l is the liquid kinematic viscosity, σ is the surface tension of the bubble/liquid interface, and E is the elastic stress.

Due to the number of time dependent components, solving equation 3 requires the simultaneous coupled solution of several differential equations. However, a qualitative description of the effects of the different parameters on the bubble growth rate can be made. First of all, increasing viscosity clearly decreases the rate of bubble expansion. Samples with large viscosities provide larger resistances to flow once melted compared to samples with lower viscosities. Thus, after a laser pulse hits the sample and heats the surface, the bubbles that nucleate in samples with high viscosity will grow to much smaller sizes over the heating duration when compared to bubbles nucleating in low viscosity samples. After the end of the pulse duration, once the melt gets quenched, samples where bubbles have grown to larger sizes will end up with larger voids within their volume. This explains the large decrease in pore size at high M_w (Figure 6) since this comes along with increasingly larger viscosities (Figure 9).

While surface tension is harder to evaluate and does not always correlate with molecular weight, it has been shown for poly(ethylene) that, similarly to viscosity, its value increases with

increasing molecular weight [36]. The value of the elastic component E depends on the model used to estimate it, such as the linear elastic, the neo-Hookean, or the Yang and Church model [37]. In our case, it can be estimated by the magnitude of the storage modulus G' . Like the previously discussed properties, G' also increases with molecular weight (Table III). In addition, its value gets closer to the loss modulus G'' with increasing M_w until eventually exceeding it for grade 7. This increase in elastic behavior at the expense of viscous dissipation at high molecular weights further explains the large decrease in pore size at high M_w . Indeed, since elastic recovery is dominant for such samples, the energy required for material deformation is much higher than for lower M_w samples. The bubbles nucleated in the laser heated melt layer thus experience an extremely large resistance to growth which leads to a small pore size.

Finally, the density of the liquid should also have an effect. Looking back at Table I and Figure 6, the polymer density does not correlate with pore size for high M_w values (39 kg/mol and above). However, a closer inspection of equation 3 reveals that as viscosity, surface tension, and elastic stress decrease (in other words at low M_w), the effect of ρ_l on the bubble growth rate is magnified as the pressure term of equation 3 starts to dominate. By checking the density values in Table I, it can be seen that even though grades 2 and 3 have smaller M_w when compared to grade 4, they are also denser and thus offer less free volume according to Flory-Fox theory [38]. From this perspective, once melted, denser polymers offer less space for bubbles to grow than low density polymers and will thus end up with smaller bubbles during laser machining. This could explain why, despite their extremely low viscosity, the pores on grades 2 and 3 are smaller than those on grade 4.

In conclusion, viscoelastic melt properties have a significant effect on femtosecond laser-induced pore size on polymer surfaces. With the exception of polymers with very low molecular weights, pore size is inversely correlated with molecular weight due to the increase in forces that inhibit the bubble growth rate during explosive boiling. Thus, a good understanding of the viscoelastic properties of a polymer are crucial for the optimization of femtosecond laser-induced structures on its surface.

4. CONCLUSION

In this study, the effect of femtosecond laser machining on the crystallographic structure of HDPE was investigated. Results indicate that machining led to a local decrease in crystallinity

and the appearance of a new monoclinic phase. This constitutes evidence that femtosecond laser-induced porosity is formed as a consequence of the rapid quenching of a superheated melt layer undergoing explosive boiling. Second, increasing molecular weight was observed to lead to a decrease in laser-induced pore size. Computed tomography allowed the investigation of the internal structure of the modified surface and showed that pores are interconnected and homogeneously distributed throughout the modified volume. Finally, the effect of molecular weight on pore size was explained by measuring the viscoelastic melt properties of the studied samples. At high molecular weights, the increased viscosity was determined to lead to lower bubble growth rates during explosive boiling, and thus to lower laser-induced pore sizes. By contributing to the current knowledge of the mechanisms behind the formation of femtosecond laser-induced porosity, this study will thus help the future optimization of pore size for omniphobic materials such as SLIPS or biomedical implants such as grafts and scaffolds.

Funding information

This work was supported by the National Sciences and Research Council of Canada (NSERC).

References

- [1] R.R. Gattass, E. Mazur, Femtosecond laser micromachining in transparent materials, *Nature Photonics*, 2 (2008), p. 219.
- [2] H. Kumagai, K. Midorikawa, K. Toyoda, S. Nakamura, T. Okamoto, M. Obara, Ablation of polymer films by a femtosecond high- peak- power Ti:sapphire laser at 798 nm, *Applied Physics Letters*, 65(14), (1994), p. 1850.
- [3] S.M. Eaton, C.D. Marco, R. Martinez- Vazquez, R. Ramponi, S. Turri, G. Cerullo, R. Osellame, Femtosecond laser microstructuring for polymeric lab- on- chips, *Journal of Biophotonics*, 5(8- 9), (2012), p. 687.
- [4] R.M. Vázquez, S.M. Eaton, R. Ramponi, G. Cerullo, R. Osellame, Fabrication of binary Fresnel lenses in PMMA by femtosecond laser surface ablation, *Optics Express*, 19(12), (2011), p. 11597.

- [5] A.A. Serafetinides, M. Makropoulou, E. Fabrikesi, E. Spyratou, C. Bacharis, R.R. Thomson, A.K. Kar, Ultrashort laser ablation of PMMA and intraocular lenses, *Applied Physics A*, 93(1), (2008), p. 111.
- [6] K.M.T. Ahmmed, C. Patience, A.-M. Kietzig, Internal and External Flow over Laser-Textured Superhydrophobic Polytetrafluoroethylene (PTFE), *ACS Applied Materials & Interfaces*, 8(40), (2016), p. 27411.
- [7] F. Liang, J. Lehr, L. Danielczak, R. Leask, A.-M. Kietzig, Robust Non-Wetting PTFE Surfaces by Femtosecond Laser Machining, *International Journal of Molecular Sciences*, 15(8), (2014), p. 13681.
- [8] Y. Jiao, C. Li, S. Wu, Y. Hu, J. Li, L. Yang, D. Wu, J. Chu, Switchable Underwater Bubble Wettability on Laser-Induced Titanium Multiscale Micro-/Nanostructures by Vertically Crossed Scanning, *ACS Applied Materials & Interfaces*, 10(19), (2018), p. 16867.
- [9] G. Li, Z. Zhang, P. Wu, S. Wu, Y. Hu, W. Zhu, J. Li, D. Wu, X. Li, J. Chu, One-step facile fabrication of controllable microcone and micromolar silicon arrays with tunable wettability by liquid-assisted femtosecond laser irradiation, *RSC Advances*, 6(44), (2016), p. 37463.
- [10] S. Baudach, J. Kruger, W. Kautek, Femtosecond Laser Processing of Soft Materials, *The Review of Laser Engineering*, 29(11), (2001), p. 705.
- [11] F. Baset, A. Villafranca, J.M. Guay, R. Bhardwaj, Femtosecond laser induced porosity in poly-methyl methacrylate, *Applied Surface Science*, 282 (2013), p. 729.
- [12] Y. Assaf, A.-M. Kietzig, Optical and chemical effects governing femtosecond laser-induced structure formation on polymer surfaces, *Materials Today Communications*, 14 (2018), p. 169.
- [13] J. Yong, F. Chen, Q. Yang, Y. Fang, J. Huo, J. Zhang, X. Hou, Nepenthes Inspired Design of Self- Repairing Omniphobic Slippery Liquid Infused Porous Surface (SLIPS) by Femtosecond Laser Direct Writing, *Advanced Materials Interfaces*, 4(20), (2017), p. 1700552.
- [14] B. Mattiasson, A. Kumar, I. Galaev, Macroporous polymers : production properties and biotechnological/biomedical applications, CRC Press/Taylor & Francis, Boca Raton, 2010.
- [15] M. Castillejo, E. Rebollar, M. Oujja, M. Sanz, A. Selimis, M. Sigletou, S. Psycharakis, A. Ranella, C. Fotakis, Fabrication of porous biopolymer substrates for cell growth by UV laser: The role of pulse duration, *Applied Surface Science*, 258(22), (2012), p. 8919.

- [16] A. Daskalova, C.S.R. Nathala, I. Bliznakova, E. Stoyanova, A. Zhelyazkova, T. Ganz, S. Lueftenegger, W. Husinsky, Controlling the porosity of collagen, gelatin and elastin biomaterials by ultrashort laser pulses, *Applied Surface Science*, 292 (2014), p. 367.
- [17] A. Miotello, R. Kelly, Critical assessment of thermal models for laser sputtering at high fluences, *Applied Physics Letters*, 67(24), (1995), p. 3535.
- [18] T. Efthimiopoulos, C. Kiagias, G. Heliotis, E. Helidonis, Evidence of volume bubble creation during laser ablation of PMMA organic polymer, *Canadian Journal of Physics*, 78(5-6), (2000), p. 509.
- [19] S. Baudach, J. Bonse, J. Krüger, W. Kautek, Ultrashort pulse laser ablation of polycarbonate and polymethylmethacrylate, *Applied Surface Science*, 154-155 (2000), p. 555.
- [20] J.M. Guay, A. Villafranca, F. Baset, K. Popov, L. Ramunno, V.R. Bhardwaj, Polarization-dependent Femtosecond Laser Ablation of Poly-methyl Methacrylate, *New Journal of Physics*, 14(8), (2012), p. 085010 (17 pp.).
- [21] S.I. Anisimov, N.A. Inogamov, A.M. Oparin, B. Rethfeld, T. Yabe, M. Ogawa, V.E. Fortov, Pulsed laser evaporation: equation-of-state effects, *Applied Physics A*, 69(6), (1999), p. 617.
- [22] W. Jia, Y. Luo, J. Yu, B. Liu, M. Hu, L. Chai, C. Wang, Effects of high-repetition-rate femtosecond laser micromachining on the physical and chemical properties of polylactide (PLA), *Optics Express*, 23(21), (2015), p. 26932.
- [23] A. Shibata, S. Yada, M. Terakawa, Biodegradability of poly(lactic-co-glycolic acid) after femtosecond laser irradiation, *Scientific Reports*, 6 (2016), p. 27884.
- [24] E. Rebollar, G. Bounos, M. Oujja, S. Georgiou, M. Castillejo, Effect of Molecular Weight on the Morphological Modifications Induced by UV Laser Ablation of Doped Polymers, *The Journal of Physical Chemistry B*, 110(33), (2006), p. 16452.
- [25] Y. Assaf, A.-M. Kietzig, Formation of porous networks on polymeric surfaces by femtosecond laser micromachining, *Proc. SPIE* 10092, 2017, p. 100920.
- [26] J.-C. Yen, F.-J. Chang, S. Chang, A new criterion for automatic multilevel thresholding, *IEEE Transactions on Image Processing*, 4(3), (1995), p. 370.
- [27] K. Tashiro, I. Tanaka, T. Oohara, N. Niimura, S. Fujiwara, T. Kamae, Extraction of Hydrogen-Atom Positions in Polyethylene Crystal Lattice from Wide-Angle Neutron Diffraction Data Collected by a Two-Dimensional Imaging Plate System: Comparison with the X-ray and Electron Diffraction Results, *Macromolecules*, 37(11), (2004), p. 4109.

- [28] R.J. Weiss, C.R. Desper, Correspondence: Structure of polyethylene, *The Philosophical Magazine: A Journal of Theoretical Experimental and Applied Physics*, 30(2), (1974), p. 441.
- [29] R. Caminiti, L. Pandolfi, P. Ballirano, Structure of Polyethylene from X-Ray Powder Diffraction: Influence of the Amorphous Fraction on Data Analysis, *Journal of Macromolecular Science, Part B*, 39(4), (2000), p. 481.
- [30] L. Fontana, D.Q. Vinh, M. Santoro, S. Scandolo, F.A. Gorelli, R. Bini, M. Hanfland, High-pressure crystalline polyethylene studied by x-ray diffraction and ab initio simulations, *Physical Review B*, 75(17), (2007), p. 174112.
- [31] K.E. Russell, B.K. Hunter, R.D. Heyding, Monoclinic polyethylene revisited, *Polymer*, 38(6), (1997), p. 1409.
- [32] H. Hu, X. Wang, H. Zhai, High-fluence femtosecond laser ablation of silica glass: effects of laser-induced pressure, *Journal of Physics D: Applied Physics*, 44(13), (2011), p. 135202.
- [33] N.M. Bulgakova, V.P. Zhukov, S.V. Sonina, Y.P. Meshcheryakov, Modification of transparent materials with ultrashort laser pulses: What is energetically and mechanically meaningful?, *Journal of Applied Physics*, 118(23), (2015), p. 233108.
- [34] Y. Bellouard, M.-O. Hongler, Femtosecond-laser generation of self-organized bubble patterns in fused silica, *Optics Express*, 19(7), (2011), p. 6807.
- [35] R. Gaudron, M.T. Warnez, E. Johnsen, Bubble dynamics in a viscoelastic medium with nonlinear elasticity, *Journal of Fluid Mechanics*, 766 (2015), p. 54.
- [36] H.W. Starkweather, The surface tension of polyethylene, *Polymer Engineering & Science*, 5(1), (1965), p. 5.
- [37] X. Yang, C.C. Church, A model for the dynamics of gas bubbles in soft tissue, *The Journal of the Acoustical Society of America*, 118(6), (2005), p. 3595.
- [38] T. Fox, P.J. Flory, Second- Order Transition Temperatures and Related Properties of Polystyrene. I. Influence of Molecular Weight, *Journal of Applied Physics*, 21(6), (1950), p. 581.